

Contents

| | | |
|----------|--|-----------|
| 1 | Nuclear fragmentation in hadron-therapy | 3 |
| 1.1 | Introduction: Radiotherapy and hadron-therapy | 3 |
| 1.1.1 | Biological advantages in hadron-therapy | 7 |
| 1.2 | Physics for hadron-therapy | 10 |
| 1.2.1 | Stopping Power of high energy ions | 11 |
| 1.2.2 | Range Stragglng and lateral beam spread | 13 |
| 1.3 | Nucleus-Nucleus collisions and Nuclear Fragmentation | 13 |
| 1.3.1 | Theoretical model of nuclear fragmentation | 18 |
| 1.3.2 | Fragmentation cross sections measurements | 18 |
| 2 | The FIRST experiment | 19 |
| 2.1 | Introduction | 19 |
| 2.2 | The experimental setup | 22 |
| 2.2.1 | The Interaction Region | 24 |
| 2.2.2 | The Large Detector Region | 25 |
| 2.2.3 | The DAQ and the trigger | 26 |
| 2.2.4 | The Monte Carlo simulation | 26 |
| 3 | FIRST Analysis | 27 |

| | | |
|----------|--|-----------|
| 3.1 | The reconstruction algorithm | 27 |
| 3.1.1 | The ZID algorithm from the TOFWALL | 27 |
| 3.1.2 | Improving the reconstruction algorithm with VD cluster size . | 27 |
| 3.2 | The angular and momentum resolutions | 27 |
| 3.3 | The reconstruction efficiencies | 27 |
| 3.4 | The double differential cross-sections | 27 |
| 4 | A possible upgrade for the FIRST detector | 29 |
| 4.1 | Improving the FIRST tracking capability with FINUDA drift chambers | 29 |
| 4.1.1 | Monte Carlo Simulation | 29 |
| 4.1.2 | FINUDA drift chambers test with cosmic rays | 29 |
| | Bibliography | 30 |

Chapter 1

Nuclear fragmentation in hadron-therapy

1.1 Introduction: Radiotherapy and hadron-therapy

The development of particle accelerators in the last fifty years towards energies higher and higher has enabled the current knowledge about matter and the fundamental interactions. Since the X-rays discovery by W.C. Roentgen in 1895 the couple between technologies developed for the fundamental research and the medical applications has been evident: shortly after the discovery, X-rays were also applied in therapy for malignant tissues. Starting from X-rays tubes in the first years of 1900 and passing through electron accelerator after the Second World War, nowadays proton and light ions accelerators present a major interest in the field of the medical application, in particular for the radiation oncology.

Because their nature and their biological interactions were not known at that time, X-rays were first used on a very empirical basis: for a long time radiation therapy remained a more or less empirical science where the major progress originated from clinical application, although laboratory research widened the scientific horizon dramatically. In the historical development of radiotherapy is evident that the clinical results are improved by a greater conformity of the applied radiation to the target

volume and by increased biological effectiveness of the radiation. In radiotherapy the key problem is to deliver the dose in such a way that ideally the planned target volume receives 100 per cent of the dose needed to kill all cancer cells in the tumor, while the surrounding tissues should not receive any dose. In practice this cannot be achieved because of the unavoidable dose deposition in the entrance channel of the radiation.

The X-rays therapy is used systematically since the seventies. The main drawback of this treatment means is the ballistics of the X-rays. As shown in Fig.1.1, which shows the dose deposition induced by different projectiles with respect to the penetration depth in liquid water, the low energy X-rays dose profile shows a steep exponential decrease with depth: the maximum of the deposition is located at a small penetration depth, near the entrance surface. It is difficult to accurately sight tumors deeply located in the body while preserving simultaneously the surrounding tissues. In the past 50 years much progress has been made to improve dose delivery towards the ideal situation and to thereby increase the tumor control rate. These achievements have been possible thank to the interdisciplinary collaboration of scientists in the fields of nuclear physics, accelerator technology, engineering, oncology and radiation medicine and biology. In order to overcome the limitations of an exponentially decreasing depth dose distribution of electromagnetic radiation numerous techniques have been developed and applied. To reduce the dose to the healthy tissues in front of the target volume, the energy of the photons was increased for the treatment of deep-seated tumors. The originally used X-rays tubes were replaced by high energy gamma rays, after ^{60}Co sources could be produced in nuclear reactors (gamma rays of 1.17 MeV and 1.33 MeV). Years later, the ^{60}Co sources have been replaced by compact linear accelerators which deliver high energy X-rays and gamma rays. In these accelerators electrons are accelerated and send to a conversion target: photons are produced by the bremsstrahlung process induced by the slowing down of the high energy electrons in the conversion target. The resulting photons beam have an energy of about 15-20 MeV that deliver a radiation dose in the patient that slow down exponentially after a maximum shifted of some centimeters from the input surface. For these high energy photons (mostly used in conventional therapy nowadays) the

initial dose build-up is mainly caused by forward scattered Compton electrons that transport some of the transferred energy from the surface to greater depth yielding an increase in dose in the first few centimeters. In this way the maximum delivered dose is distant respect to the patient flesh that is particularly photo-sensitive, saving it by radiation damage. In addition, the exponential decay becomes less steep improving the ratio of entrance dose to target dose for the treatment of deep-seated tumors.

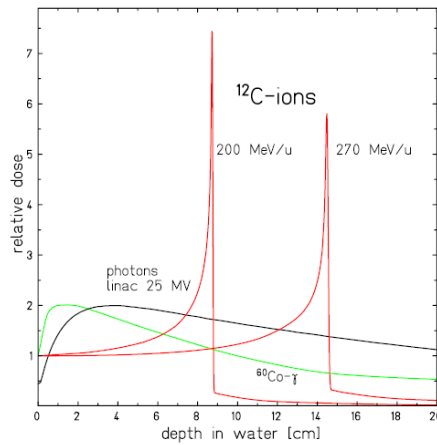


Figure 1.1: Dose profile for different photons and carbons beams energies

In order to improve X-rays therapy efficiency in adapting the dose to the tumor volume, several irradiation procedures have been developed during the last decades: the Intensity Modulated Radio Therapy (IMRT), the Cyberknife and the Tomotherapy. The IMRT uses 6-10 X-rays beams and multi-leaf collimators in order to conform the irradiation field to the external shape of the tumor. The intensity and the direction of each beam are optimized according to a complex system of software (TPS: Treatment Planning System) in such a way to have the minimum dose delivered in healthy tissues respect to a given therapeutic dose delivered to the tumor. The Cyberknife is a very compact low energy accelerator mounted on a robot: this allows to use different beam incidences in 3D and hence concentrate the delivered dose on the tumor while spreading the dose on healthy tissues. The Tomotherapy is

an extension of the IMRT which uses all possible incidences in a plane, the beam intensity depending of the beam incidence. In other techniques, radioactive sources of low range emitters are implanted directly into the tumor to achieve a target-conform exposure. In general, all these techniques yielded better clinical results when the tumor is exposed to a greater dose without increasing the dose delivered to the normal tissues. The dose delivered for each treatment in the correspondence of the tumor volume is about 2 Gy ($1\text{Gy} = 1 \text{ J/Kg}$). The whole treatment is composed of 30-35 sessions, generally distributed in 6-7 weeks, with a total delivered dose of 60-70 Gy. These techniques are nowadays widely used all around the world and the therapists have now a good experience of X-rays therapy. The X-rays therapy is used as a reference to study the efficiency of other particle therapies. Nowadays radiotherapy plays an important role in the treatment of cancer. After surgery it is the most frequently and most successfully applied form of therapy. More than 50% of all patients with localized malignant tumors are treated with radiation. However the total cure rate, obtained by using combinations of different therapeutic means (the surgery, the chemotherapy and the X-rays therapy) is just around 45%. The main reasons for the failure of the treatments for the 55% of the patients, are the lack of local control on the tumor and the development of metastases.

While the potential of X-rays for treating cancer was recognized soon after their discovery in 1895, it was not until 1946 that Robert R. Wilson proposed that high energy beams of heavy charged particles like protons and light ions could be used for localized cancer therapy, based on their favorable tissue depth-dose distribution. In fact he investigated the depth dose profile of protons produced at the Berkeley cyclotron and observed a steep increase of energy deposition i.e. of dose at the end of the particle range [1]. This increase in ionization density had been already measured in 1903 by Bragg for alpha particle in air and is known as Bragg profile [2]. It is evident that the increase in ionization density towards the end of the particle trajectory allows to transport a higher dose to a deep seated tumor than would be possible using conventional photons beams: by contrast with X-rays, which are absorbed by the body and show an exponential decrease in the radiation dose with increasing tissue depth, charged particles deposit little energy at the body's surface

(from 10% to 20% of the maximum), when their velocity is high, and instead deposit most of their energy just before they come to rest in tissue (Fig.1.1). As it will be seen later, calibrating accordingly the initial energy of the beam is possible to deliver the dose at different depths: the location of the Bragg peak only depends on the particle incident energy. In Fig.1.1 are shown the dose profiles of two Carbon ions beam at the initial kinetic energy of 250 MeV/u and 300 MeV/u (with MeV/u here indicate MeV/nucleon). Since the Bragg peak for particles of a given energy is very narrow, different beam energies are necessary to paint the volume of a tumor: the plateau resulting from the combination of different beam energies is called the Spread Out Bragg Peak (labeled SOBP), as illustrated in Fig.1.2. In that case, the dose deposition before the SOBP may be quite large (more than 50% of the maximum) depending on the size of the tumor and the number of beams used to paint it.

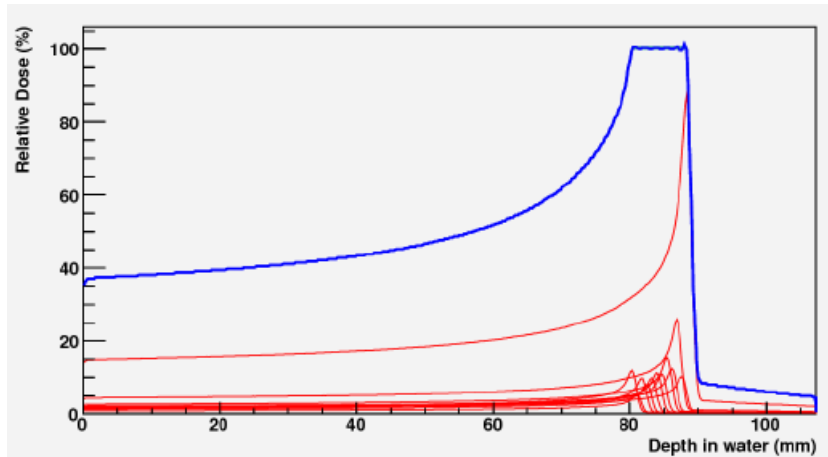


Figure 1.2: Spread-out Bragg peak

1.1.1 Biological advantages in hadron-therapy

Another advantage of the particle therapies lies in the biological effects induced by the charged particles. To kill the same amount of cells lower doses are needed

compared to X-rays. This effect is parametrized by the Relative Biological Efficiency factor (RBE). It is defined as the ratio of the Dose D_γ needed to kill a given amount of cells for X-rays to the dose D_{part} needed to kill the same amount of cells for the particle under interest:

$$RBE = \frac{D_\gamma}{D_{part}} \quad (1.1)$$

The Fig.1.3 shows different survival curves (the rate of surviving cells with respect to the dose) for photons (full line) and for heavy ions (dashed line). It is seen that depending on the survival rate, the RBE can range from 1.5 to 2.1. The average RBE is around 1.1 for protons. The assumed RBE value for carbons is around 3.

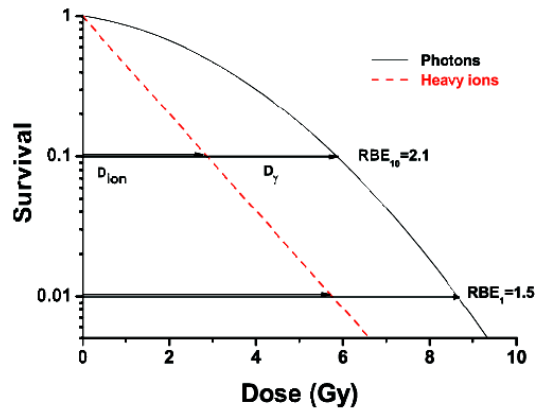


Figure 1.3: Survival curves and relative RBE for cells inactivation for 10% and 1% survival level for a typical heavy ion irradiation

Another biological effect is the so called *Oxygen Effect*: the cells with a low oxygenation rate (hypoxic cells) are more resistant to radiations than cells with a normal oxygenation rate (normoxic or aerobic cells). As a consequence, more dose is needed to destroy hypoxic cells. Unfortunately resistant hypoxic cells are located in the cancer tumors. This effect is parametrised by the *Oxygen Enhancement Ratio* (OER) which is defined as follows:

$$OER = \frac{D_{hypoxic}}{D_{aerobic}} \quad (1.2)$$

where $D_{hypoxic}$ is the dose needed for heavy ions to kill a fixed amount of hypoxic cells and $D_{aerobic}$ is the dose needed to kill the same amount of aerobic cells. The Fig.1.4 shows the survival curves for particle with different Linear Energy Transfer (LET) values for aerobic cells (full lines) and hypoxic cells (dashed lines). The OER value clearly depends on the LET value. For X-rays the OER values is around 3. For particles with low LET values like carbo ions at high energies, the OER value is around 2.6. For high LET values like carbon at low energies, close to the Bragg peak, the OER value decreases down to 2.

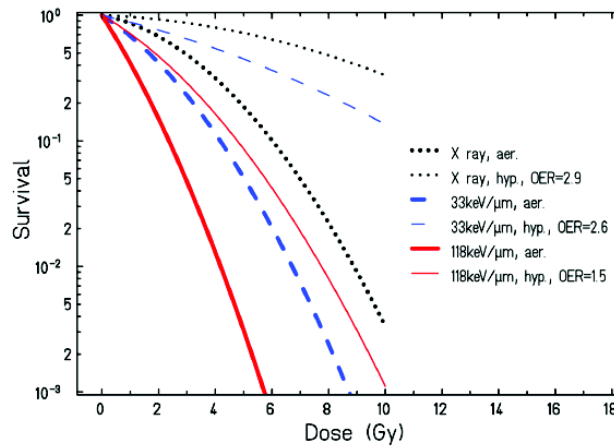


Figure 1.4: Influence of the oxygen level on cell survival of human kidney T-1 cells for carbon ions with different LET

RBE and OER values are summarized on Fig.1.5. One can see that the main improvement in using protons for radiation therapy is the ballistics of protons since the RBE value is only 1.1 and the OER value is close to the OER value of X-rays. The RBE value increases with the size of the ion and the OER value decreases with the size of the ion. For the ions heavier than neon the OER value is close to one: the Oxygen Effect has almost disappeared. A major improvement in radiation therapy

1.2. PHYSICS FOR HADRON-THERAPY

may be achieved by using heavy ions: less dose is necessary to kill cancerous cells and no additional dose is needed to kill hypoxic radio-resistant cells. One can also notice that neutrons are very efficient in killing cancerous cells. Unfortunately, neutrons have a very poor ballistics and an accurate sighting of a tumor is very difficult.

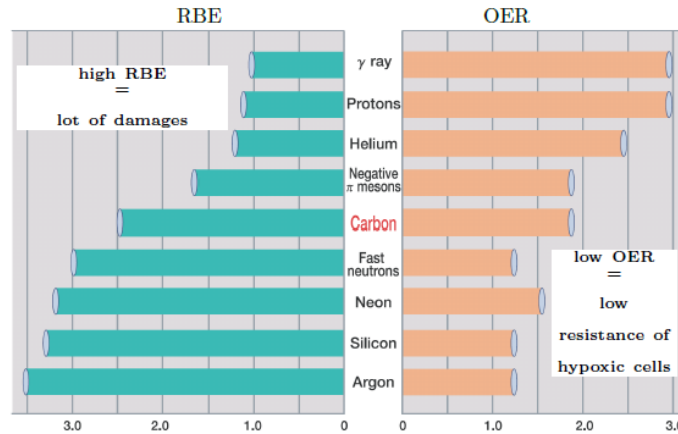


Figure 1.5: RBE (left) and OER (right) values of different particles

All these physical (ballistics) and biological (high RBE and low OER values) properties make heavy ions good candidates for their use in radiation therapy. They will be used for cancers with a low success rate with conventional therapeutic means. The main indications for charge particle therapy are radio resistant and inoperable tumors like brain, head and neck tumors. These properties of proton and ions beams can be used in order to overcome the physical and biological limitations of the conventional radiotherapy. The therapy that uses hadrons beams to irradiate malignant tissues is called hadrontherapy, to distinguish it from the traditional X-rays and γ -rays therapy, usually called just radiotherapy.

1.2 Physics for hadron-therapy

As shown in last section, the main reason for using heavy charged particles in radiotherapy is their favorable depth-dose profile: charged particles beams have a better

ballistics than photons. The use of charged particles for therapeutic purposes requires a very drastic dose control: the Bragg peak location has to be known within 1 mm and the dose in the tumor has to be delivered within 3%. To do that properly is necessary to show the basic physical concepts which are necessary to compute the dose deposition and the range of charge particles in matter.

1.2.1 Stopping Power of high energy ions

The dose deposited in tissue is the most important physical quantity in radiotherapy. It is defined [3] by the term absorbed dose (unit Gray [Gy]) as the mean energy $d\epsilon$ deposited by ionizing radiation in a mass element dm :

$$D = \frac{d\epsilon}{dm} \quad [1 \text{ Gy} = 1 \text{ J/Kg}] \quad (1.3)$$

In radiation therapy (RT) water is used as tissue reference medium. A more operational definition is used:

$$D = \frac{N}{dS} \frac{(dE/dx)}{\rho} \quad (1.4)$$

where N/dS is the fluency of the beam and dE/dx is the stopping power of the particle in the matter and ρ the material's density. Since the fluency can be measured and the material's density is known, one only has to know the stopping power to compute the physical dose. All the physics lies in the computation the stopping power.

Radiotherapy of deep-seated tumors requires ion beam ranges in tissue of up to 30 cm corresponding to specific energies up to 220 MeV/u for protons and helium ions, 430 MeV/u for carbon ions, and 600 MeV/u for neon ions with particle velocities $\beta = v/c \approx 0.7$. At these velocities the energy-loss rate dE/dx in the slowing-down process is dominated by inelastic collisions with the target electrons and can be

1.2. PHYSICS FOR HADRON-THERAPY

well described by the Bethe-Bloch formula, here given in the relativistic form (with $M_{projectile} \gg m_e$) described by Fano [4], including the shell correction term C/Z , and the density effect correction term $\delta/2$:

$$\frac{dE}{dx} = \frac{4\pi e^4 Z_t Z_p^2}{m_e v^2} \left[\ln \frac{2m_e v^2}{\langle I \rangle (1 - \beta^2)} - \beta^2 - \frac{C}{Z_t} - \frac{\delta}{2} \right] \quad (1.5)$$

Z_p and Z_t denote the nuclear charges of the projectile and the target, m_e and e are the mass and charge of the electron, and $\langle I \rangle$ is the mean ionization energy of the target atom or molecule that is of crucial importance since it rules the energy loss of the projectile and its range. It can be determined from experimental data. For liquid water the values obtained from energy-loss measurements for protons and different heavier ions are in the range $\langle I \rangle = 75 - 78 eV$ [5, 6, 7, 8]. As it can be seen the stopping power in a given material depends mainly from the projectile characteristics: in this approximation the $\frac{dE}{dx}$ doesn't depend from the mass of the projectile, but only from its charge and its velocity. It increases with decreasing particle kinetic energy due to the factor $\frac{1}{\beta^2}$ and it increases with particle charge according to Z_p^2 . At high velocities the atomic electrons are completely stripped off and the projectile charge is equal to the atomic charge number Z_p . At lower velocities comparable to the velocity of the orbital electrons of the material (for light ions below about 10 MeV/u) the stopping-power reaches a maximum and then drops sharply again. Here a number of complicated effects come into play, the most important of which is the tendency of the particle to pick up electrons: the mean charge state decreases due to the interplay of ionization and recombination processes and Z_p in Bethe-Bloch formula has to be replaced by the effective charge Z_{eff} , which can be described by the empirical formula:

$$Z_{eff} = Z_p [1 - \exp(-125\beta Z_p^{-2/3})] \quad (1.6)$$

This effect decrease the effective charge and so the stopping power of the projectile.

At still lower projectile energies ($E_p \leq 10\text{keV}/u$) elastic Coulomb collisions with target nuclei begin to contribute significantly to the energy loss and dominate the stopping process at the very end of the particle path i.e. for the last few μm . The corresponding dose contribution is however very small and can be neglected in hadron-therapy applications. The major effect of Coulomb scattering is the angular deflection of the particle along its path, according to the $\frac{1}{\sin^4(\frac{\theta}{2})}$ dependence of the Rutherford formula for a single collision. This is true especially for light particle respect to target nuclei, when the small energy transfer to the nucleus is negligible so that the scattering is elastic. When a particle traverses a thick block of material the number of collisions grows up and usually we speak about Multiple Coulomb scattering. The cumulative effect of these small angle scatterings is, however, a net deflection from the original particle direction.

Another process to take in account for ion projectiles is the nucleus-nucleus collision which produces secondary particles with longer ranges than the projectile. This process influence significantly the dose map and become more and more important with the increasing of the ion mass number A .

Stopping power curves for protons and ^{12}C ions in water are shown in Fig.1.6. For protons, the inelastic collision on the electrons is the dominant process for all energies. For ^{12}C ions this process is also dominant except for the last few micrometers of path where the nucleus-nucleus interactions become dominant; the maximum occurs at a specific energy of $\approx 350\text{keV}/u$.

1.2.2 Range Straggling and lateral beam spread

1.3 Nucleus-Nucleus collisions and Nuclear Fragmentation

While the stopping process of high energy ions penetrating a thick absorber is governed by collisions with atomic electrons, the probability of nuclear reactions is much smaller, but leads to significant effects at large penetration depths. At energies of

1.3. NUCLEUS-NUCLEUS COLLISIONS AND NUCLEAR FRAGMENTATION

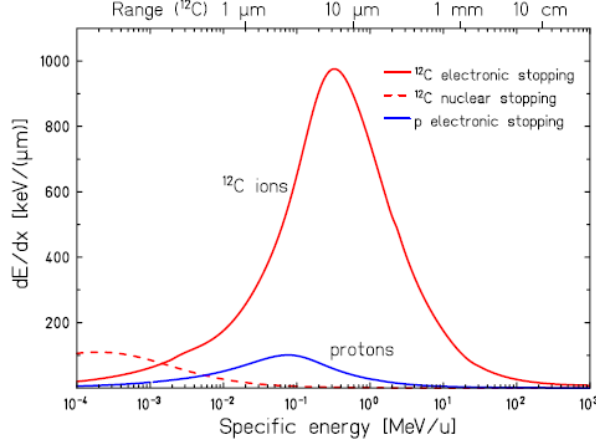


Figure 1.6: Stopping power curves for protons and ^{12}C ions in water. The range of ^{12}C ions in water corresponding to their specific energy is indicated at the top

several hundred MeV/u violent nuclear spallation reactions may result in a complete disintegration of both projectile and target nuclei (e.g. in central head-on collisions), or in partial fragmentations. For geometrical reasons peripheral collisions, where the beam particle loses one or several nucleons, are the most frequent nuclear reactions occurring along the stopping path of the ions. The nucleus-nucleus collisions can be schematically described as follows as shown on 1.7. When a projectile hits a target nucleus (panels a) and b)), light particles are promptly emitted and an excited quasi-projectile and an excited quasi-target are formed (panel c)). These excited nuclei decay through consecutive light particle emissions (*evaporation process*) or by a simultaneous break-up (*fragmentation process*). The first step of this description is called the *entrance channel phase* (panels a),b) and c)) and the second step is called the *decay phase* (panels d),e) and f)). For both steps, several models have been developed. A complete nucleus-nucleus collision modeling is achieved by a combination of a model describing the entrance channel and a model describing the decay phase.

Nucleus-nucleus collisions will have two main effects. The first one is the disap-

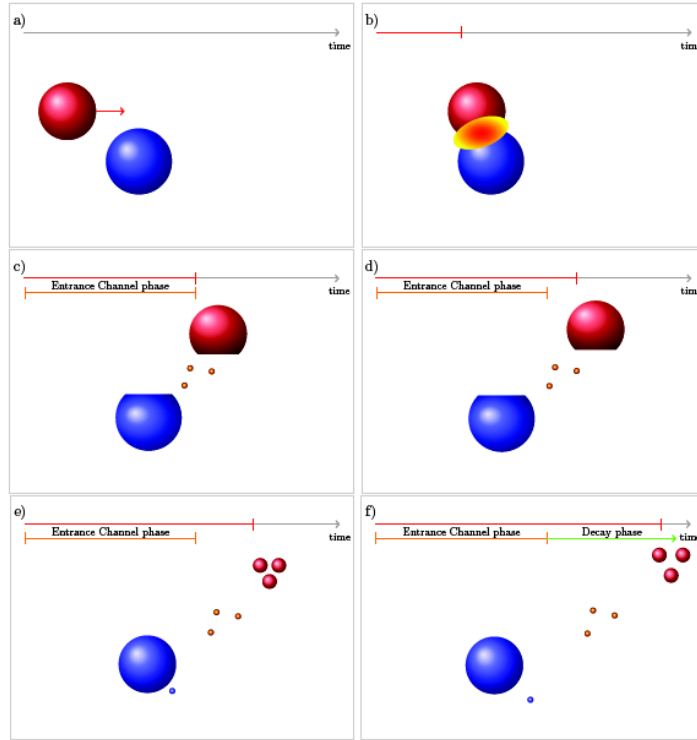


Figure 1.7: Schematic view of a nucleus-nucleus collision

pearance of the projectile since the collision will change its nature. As a consequence, this projectile will not deposit its energy up to the Bragg Peak. The second effect is the secondary particle production. These fragments will be often of smaller size but with a velocity close to velocity of the projectile. Because of the $\frac{A}{Z^2}$ scaling of the range for particles with the same velocity, these fragments will deposit their energy at penetration depths beyond the projectile Bragg Peak.

Let us see how those effects manifest for protons and ^{12}C ions. The 1.8 shows the ratio of projectiles which have not experienced a nuclear collision on a nucleus of the absorber with respect to the penetration depth for 150 MeV proton in liquid water (left panel) and the Bragg Curve for 150 MeV protons in liquid water (right panel). This figure results from GEANT4 simulations. On both panels, the black curve corresponds to simulations in which the nucleus-nucleus collision process has

1.3. NUCLEUS-NUCLEUS COLLISIONS AND NUCLEAR FRAGMENTATION

not been considered (label EM: only inelastic scattering with electron is considered i.e. only e.m. interactions) and the red curves to simulations in which the nucleus-nucleus collision process has been activated (label NUC). The effect of the projectile consumption is clearly seen on 1.8. Whereas all projectiles reach the Bragg Peak for EM simulations, only 80% of them reach for NUC simulations. As a consequence, the energy deposition at the Bragg Peak (see left panel of 1.8) is reduced by 20% for NUC collisions compared to EM collisions. Nuclear collisions have no effect on the location of the Bragg Peak which is driven by the Bethe-Bloch equation only. The contribution of secondary fragments, i.e. an energy deposition beyond the Bragg Peak, is not directly seen (see right panel of 1.8). Secondary fragments are issued from the target only. Their velocity is very small and hence their range do not exceed few micro-meters. They deposit their energy close to the collision location. The indirect effect lies in the total amount of energy which has been deposited in the absorber. Since some energy is needed to produce fragments, each time a proton collides on a nucleus, one part of the total energy of the system is exhausted in the particle production. As a result, the integral of the Bragg Curve for NUC simulations is only 97% of the projectile incident energy, whereas this integral is equal to the projectile incident energy for EM simulations.

The influence of the nucleus-nucleus reactions on the dose deposition for ^{12}C ions is very similar as it can be observed on 1.9 which has been obtained for 290 MeV/u ^{12}C ions using the GEANT4 simulation framework. But in this case only 50% of projectiles reach the Bragg Peak (see left panel of 1.9), leading to a reduction of 50% on the energy deposition per incident ^{12}C at the Bragg Peak (right panel of 1.9). The ratio of ^{12}C ions which do not experience a nuclear interaction decreases exponentially with respect to the penetration depth. As for protons, the locations of the Bragg Peaks are identical for EM and NUC simulations. The integral of Bragg Curve is equal to 93% of the incident energy for NUC simulations. The difference compared to protons is the energy deposition tail beyond the Bragg Peak. As for protons, the fragments emitted by the target nucleus have a very short range and deposit locally their energy. The fragments emitted by the fragmenting projectile have

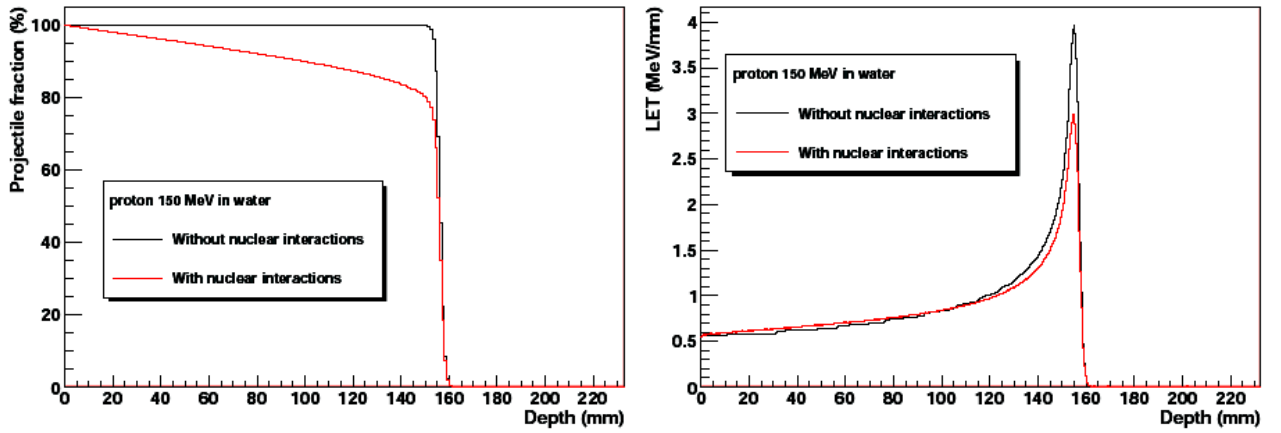


Figure 1.8: Schematic view of a nucleus-nucleus collision

a velocity close to the projectile velocity and hence a longer range. Due to the $\frac{A}{Z^2}$ scaling of the ranges, fragments with a size close to the projectile size (namely $Z=3$ to $Z=6$ fragments) will have a range close to the range of the projectile. Lighter fragments will have a much longer range. The tail seen on 1.9, also called the *fragmentation tail*, results mainly from the contribution of hydrogen and helium isotopes.

These simulations show clearly that the dose map is significantly changed when the nucleus-nucleus collisions are taken into account.

Some important conclusions can be drawn for the effects of fragmentation relevant to radiotherapy with high-energy ion beams: 1) Nuclear reactions cause a loss of primary beam particles and a buildup of lower- Z fragments, these effects becoming more and more important with increasing penetration depth. 2) The secondary projectilelike fragments are moving with about the same velocity as the primary ions. They have in general longer ranges and produce a dose tail behind the Bragg peak. 3) The angular distributions of fragments are mainly determined by reaction kinematics and forward directed, but much broader than the lateral spread of the primary ions caused by multiple Coulomb scattering [9, 10].

1.3. NUCLEUS-NUCLEUS COLLISIONS AND NUCLEAR FRAGMENTATION

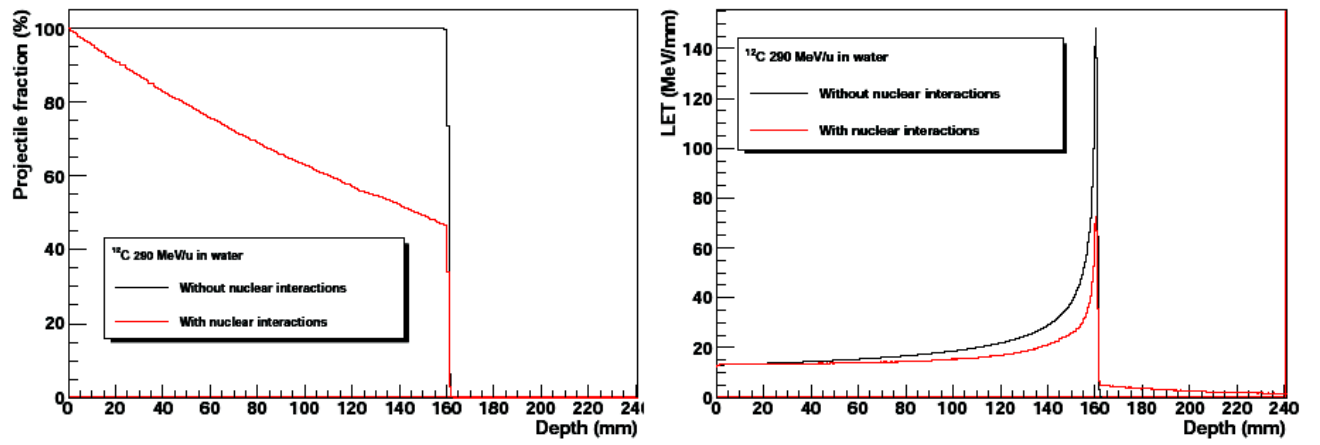


Figure 1.9: Schematic view of a nucleus-nucleus collision

1.3.1 Theoretical model of nuclear fragmentation

1.3.2 Fragmentation cross sections measurements

Chapter 2

The FIRST experiment

2.1 Introduction

The goal of FIRST (Fragmentation of Ions Relevant for Space and Therapy) experiment is to measure the double differential ions fragmentation cross-sections at different angles and energies between 100 MeV/u and 1000 MeV/u. This measure in this range of energies is of great interest for the applications of particle therapy in oncology and radiation protection in space missions.

Nuclear fragmentation cross-sections are essential for accurate treatment planning, as only roughly 50% of the heavy ions directed to the patient actually reach a deep tumor [11]. Treatment plans are generally based on algorithms that deal with the transport of energetic charged particle in matter. These algorithms can be described either by deterministic codes, based on Boltzmann-type transport equations, or by Monte Carlo (MC) codes that sample the interaction process on a event-by-event basis, and both approaches rely on nuclear interaction cross-sections. The cross-sections required for transport involve total yields and multiplicities and inclusive secondary energy spectra for one-dimensional transport or inclusive double-differential cross-sections in angle and energy for three-dimensional transport. For MC simulations, exclusive cross-sections may be needed for computer algorithms. In the last chapter we see that the use of charged particles for medical treatment

planning need to be careful to spare the normal tissues surrounding the tumors. This requires a great accuracy: the Bragg peak location has to be known within 1 mm and the dose in the tumor has to be delivered within 3%. Treatment plans are generally based on deterministic codes, but the great accuracy required makes necessary several inter-comparisons of the codes with MC calculations [12, 13, 14, 15, 16]. All these calculations are based on measured nuclear fragmentation cross-sections of carbon ions in water or tissue-equivalent materials, mostly performed in the past in USA (BEVALAC and Berkeley), Japan (HIMAC in Chiba) and GSI in Germany (for a review see [17]). Most of these measurements are however limited to yields or total charge-changing fragmentation cross-sections, while the needed measurements of double-differential cross-section are scarce. Not surprisingly, while fluence and total cross-sections are well described by current computer codes, the production of light fragments and their angular distribution is affected by large uncertainties and various codes may differ up to an order of magnitude in their predictions [18].

Similar problems are found in codes used for space radiation transport in shielding materials: despite several measurements of the fragmentation cross-sections related with space radio protection (reviewed in [19]), the angular distributions are not yet well reproduced. The same goes for the production of different He isotopes, mesons, and γ -rays. NASA is currently completing a large data base [20] of measured nuclear fragmentation cross-sections including approximately 50000 datasets, and has concluded that several experimental data are missing, including double-differential cross-sections for C-ions at energies below 400 MeV/u, which are those needed also for improving treatment planning in therapy.

It is therefore concluded that accurate measurements of double-differential cross-sections of light ions in the energy range 100–500 MeV/u are urgently needed for improving transport codes to be used in cancer therapy and space radiation protection.

The start of the scientific program of the FIRST experiment was on summer 2011 at the Heavy Ion Synchrotron SIS of GSI laboratory in Darmstadt and was focused on the measurement of 400 MeV/u ^{12}C beam fragmentation on thin (8mm) carbon target.

When a light ion impinges on a target nucleus, a fragmentation process can take place depending on the impact parameter between the colliding nuclei. The target fragments usually carry little momentum, while, in particular at high energies, the projectile fragments travel at nearly the same velocity as the beam ions and have only a small deflection, except for the lighter fragments (particularly protons and neutrons). In 2.1 and 2.2 the energy and angular distribution predicted by FLUKA Monte Carlo [21, 22] for the fragments produced by a 400 MeV/u carbon beam on a carbon target are shown: the number of all the particles produced in the target for a given run in a certain energy bin (N_{prod}) divided by the number of initial C-ions (N_{primC}), normalized by the bin width (MeV/u, sr) for the energy (angular) spectra, are shown as a function of the fragment energy (angle). As it can be seen the heavy fragments are forward peaked and keep the projectile velocity, while a huge amount of neutrons and protons are spread out over a wide range of angle and energy.

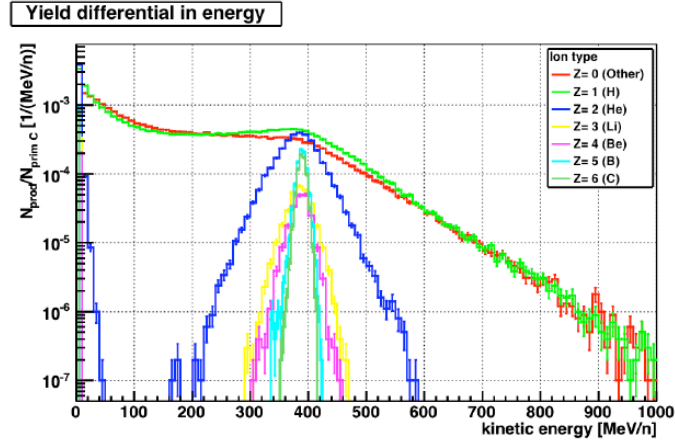


Figure 2.1: Kinetic energy distribution of the fragments produced by a 400 MeV/u carbon beam on 8 mm carbon target. $N_{prod}=N_{primC}$ is the yield of fragments per primary carbon ion (FLUKA Monte Carlo)

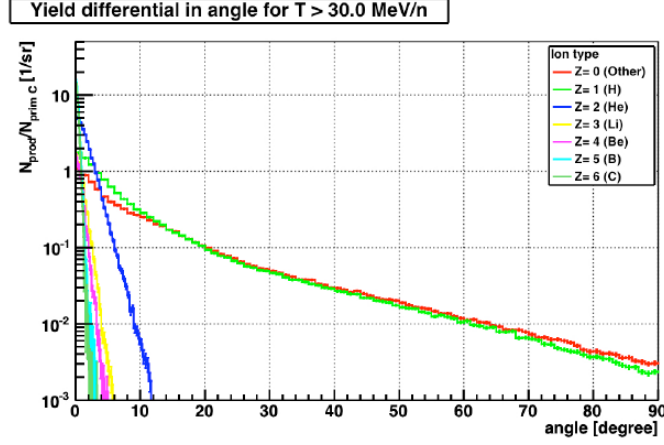


Figure 2.2: Angular distribution of the fragments produced by a 400 MeV/u carbon beam on 8 mm carbon target. $N_{prod}=N_{prim}C$ is the yield of fragments per primary carbon ion and steradian with a kinetic energy larger than 30 MeV/u (FLUKA Monte Carlo)

2.2 The experimental setup

The detector consists of several subdetectors divided in two main blocks: the Interaction Region and the Large Detector Region. The two regions are very different in dimensions of the corresponding detectors: the impinging beam and produced fragments are studied in the Interaction Region within some tens of centimeters from the target, while the devices that detect the fragments, after magnetic bending, in the Large Detector Region have typical dimension of meters. A schematic view of the FIRST experiment set up is shown in 2.3.

Following the beam path, the Interaction Region is made of a Start Counter (SC) scintillator that provides the start to the time of flight (TOF) measurement, a drift chamber Beam Monitor (BM), that measures the beam trajectory and impact point on the target, a robotized target system, a pixel silicon Vertex Detector (VD), to track the charged fragments emerging from the thin target and finally a thick scintillator Proton Tagger (KENTROS) that detects the light fragments at large

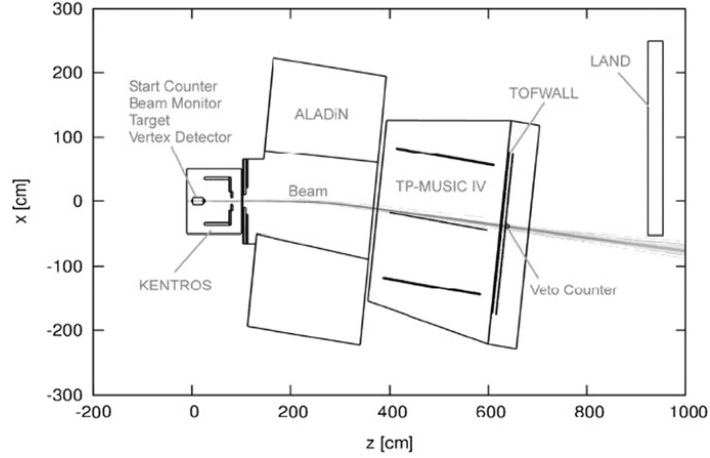


Figure 2.3: Top view of the implementation of the FIRST setup. The line shows the path of the non-interacting carbon ions

angles. With the exception of the large angle protons and a little fraction of ${}^4\text{He}$, most of the projectile fragments are produced in the forward direction with the same β of the beam 2.2. These $Z \geq 2$ fragments are within the magnetic acceptance of the ALADiN dipole magnet and after magnetic bending they enter in the Large Detector Region. Here they should have been detected by the large volume time projection chamber (TP-MUSICIV) for the measures of track directions and energy releases. Unluckily this detector didn't work during the acquisition causing not only a lost of information but also a secondary fragmentation of the beam that can determine an overestimation of the fragmentation cross-sections. A large area system of scintillators (TOFWALL) provides the measurement of the impinging point and the arrival time of the particles. The Veto Counter, a scintillator sandwich positioned after the TOFWALL in correspondence of the non-interacting beam path, is used to analyze the beam. Finally, the Large Area Neutron Detector (LAND), made of a stack of scintillator counters, gives information about the neutrons emitted within an angle of $\approx 10^\circ$ with respect to the beam.

The tracking before and after the magnetic bending, coupled with the knowledge of beam direction and impact point on the target, can provide information on the

2.2. THE EXPERIMENTAL SETUP

$\frac{p}{Z}$ ratio of the produced fragments. Care must be taken to match the information of the Interaction Region with that collected in the Large Detector Region, matching the charged ion tracks detected by VD with the clusters in the TOFWALL. A careful alignment can be achieved between these tracking devices using the copious events with non-interacting carbon ions. The main features of the beam provided by the SIS accelerator are a rate of incoming particles in the range of the kHz and a Gaussian shape in the transverse plane of 2.1 mm size (σ).

In conclusion the FIRST setup [23] fulfills several requirements: suitable particle identification capability providing a $\frac{\Delta M}{M} \leq 10\%$ (where M is the fragment mass), tracking capability to measure angles and momenta of the produced charged fragments, large angular acceptance for low energy protons, and finally angular acceptance for the forward produced neutrons. A 10% relative error on the fragment mass is mandatory in order to have a clear separation of all the ions and isotopes under study. The requirement on the fragment mass separation directly translates into performance requirements (time and momentum resolution) for all the detectors that are used in the FIRST setup.

2.2.1 The Interaction Region

In 2.4 we show a technical drawing of the Interaction Region. All the detectors of this region have been tested at the 80 MeV/u ^{12}C beam of the Superconducting Cyclotron at the Laboratori Nazionali del Sud (LNS) of the INFN or at the Beam Test Facility 510 MeV electron beam of the Frascati National Laboratory of INFN.

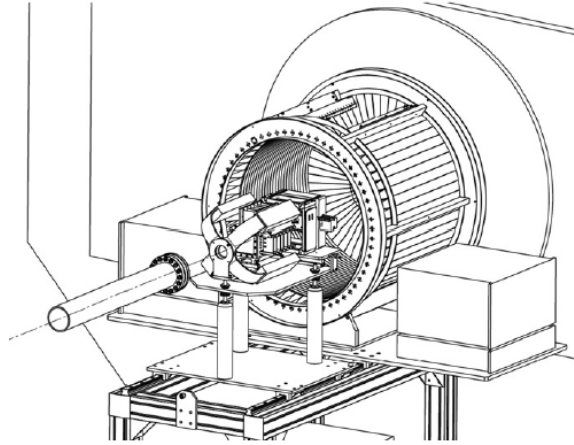


Figure 2.4: Technical drawing of the Interaction Region, embedding the Start Counter, the Beam Monitor, the Vertex Detector and the Proton Tagger. The Interaction Region is located at the entrance of the ALADiN Magnet

The Start Counter

The Beam Monitor

The Vertex Detector

The Proton Tagger

2.2.2 The Large Detector Region

The fragments produced in the forward direction in the target enter in the large detector region crossing the ALADiN [24] dipole magnet. The ALADiN field bends the charged fragments trajectory providing information about their charges and momenta. The ALADiN magnet and the other detectors of the Large Detector Region have been inherited from previous GSI experiment and have been described in detail elsewhere [24, 25, 26, 27]. Here we call their main features as far as they are needed to describe the performance of the FIRST setup.

The TOFWALL

The LAND Detector

The Veto Counter

2.2.3 The DAQ and the trigger

2.2.4 The Monte Carlo simulation

Chapter 3

FIRST Analysis

3.1 The reconstruction algorithm

3.1.1 The ZID algorithm from the TOFWALL

3.1.2 Improving the reconstruction algorithm with VD cluster size

3.2 The angular and momentum resolutions

3.3 The reconstruction efficiencies

3.4 The double differential cross-sections

3.4. THE DOUBLE DIFFERENTIAL CROSS-SECTIONS

Chapter 4

A possible upgrade for the FIRST detector

4.1 Improving the FIRST tracking capability with FINUDA drift chambers

4.1.1 Monte Carlo Simulation

4.1.2 FINUDA drift chambers test with cosmic rays

*4.1. IMPROVING THE FIRST TRACKING CAPABILITY WITH FINUDA
DRIFT CHAMBERS*

Bibliography

- [1] R.R.Wilson, *Radiological Use of Fast Protons*, Radiology 47, 487-491 (1946).
- [2] W.Bragg, *On the α particles of radium and their loss of range in passing through various atom and molecules*, Philos. Mag. 10, 318-340 (1905).
- [3] ICRU report 51: *Quantities and Units in Radiation Protection Dosimetry*, International Commission on Radiation Units and Measurements, Bethesda, MD (1993).
- [4] U.Fano, *Penetration of protons, α particles and mesons*, Annu. Rev. Nucl. Sci. 13, 1-66 (1963).
- [5] H.Bichsel, T.Hiraoka, *Energy Loss of 70 MeV protons in elements*, Nucl. Instrum. Methods. Phys. Res. B 66, 345-351 (1992).
- [6] H.Bichsel, T.Hiraoka, K.Omata *Aspect of fast-ion dosimetry*, Radiat. Res. 153, 208-213 (2000).
- [7] Y.Kumazaki, T. Akagi, T.Yanou, D.Suga, Y.Hishikawa, and T. Teshima, *Determination of the mean excitation energy of water from proton beam ranges*, Radiat. Meas. 42, 1683-1691 (2007).
- [8] H.Paul, *The mean ionization potential of water, and its connection to the range of energetic carbon ions in water* Nucl. Instrum. Methods Phys. Res. B 255, 435-437 (2007).

BIBLIOGRAPHY

- [9] Golovkov, M., D. Aleksandrov, L. Chulkov, G. Kraus, and D.Schardt, *Fragmentation of 270 AMeV carbon ions in water*, Advances in Hadrontherapy, International Congress Series No. 1144 (Elsevier Science, New York), pp. 316–324, (1997).
- [10] Matsufuji, N., M. Komori, H. Sasaki, K. Akiu, M. Ogawa, A.Fukumura, E. Urakabe, T. Inaniwa, T. Nishio, T. Kohno, and T. Kanai, *Spatial fragment distribution from a therapeutic pencil-like carbon beam in water*, Phys. Med. Biol. 50, 3393–3403, (2005).
- [11] S.Kox, et al., Physical Review C 35, 1678, (1987).
- [12] Sommerer, et al., Physics in Medicine and Biology 51, 4385, (2006).
- [13] J.Allison, et al., IEEE Transactions on Nuclear Science NS-53, 270, (2006).
- [14] M.C.Morone, et al., Physics in Medicine and Biology 53, 6045, (2008).
- [15] T.Sato, et al., Radiation Research 171, 107, (2009).
- [16] T.T.Bohlen, et al., Physics in Medicine and Biology 55(19), 5833, (2010).
- [17] D.Schardt, et al., Reviews of Modern Physics 82, 383, (2010).
- [18] J.H.Heinbockel, et al., Advances in Space Research 47, 1079, (2011).
- [19] M.Durante, F.A.Cucinotta, Reviews of Modern Physics 83, 1245, (2011).
- [20] J.W.Norbury, J.Miller, 47th NCRP Annual Meeting, Bethesda, MD, p.24, (2011).
- [21] G.Battistoni, et al., *The FLUKA code: description and benchmarking*, in: *Proceedings of the Hadronic Shower Simulation Workshop 2006*, AIP Conference Proceedings, vol.896, p.31, (2007).
- [22] A.Ferrari, P.R.Sala, A.Fasso', J.Ranft, *FLUKA: A Multi Particle Transport Code*, Technical Report CERN-2005-10, INFN/TC05/11, SLAC-R-773, (2005).

BIBLIOGRAPHY

- [23] V.Patera, Nuclear physics experiment for hadron therapy application, *Nuovo Cimento C* 34 (6)(2011).
- [24] J.Hubele, et al., *Zeitschrift fur Physik A*340, 263, (1991).
- [25] A.Schuttauf, et al., *Nuclear Physics A*607, 457, (1996).
- [26] T.Blaich, et al., *Nuclear Instruments and Methods in Physics Research Section A*314, 136, (1992).
- [27] K.Boretzky, et al., *Physical Review C* 68, 024317, (2003).